Probing Edge State Conductance in Ultra-Thin Topological Insulator Films

Arthur Leis, Michael Schleenvoigt, Kristof Moors, Helmut Soltner, Vasily Cherepanov, Peter Schüffelgen, Gregor Mussler, Detlev Grützmacher, Bert Voigtländer,* Felix Lüpke, and F. Stefan Tautz

Quantum spin Hall (QSH) insulators have unique electronic properties, comprising a band gap in their 2D interior and 1D spin-polarized edge states in which current flows ballistically. In scanning tunneling microscopy (STM), the edge states manifest themselves as an enhanced local density of states (LDOS). However, there is a significant research gap between the observation of edge states in nanoscale spectroscopy, and the detection of ballistic transport in edge channels which typically relies on transport experiments with microscale lithographic contacts. Here, few-layer films of the 3D topological insulator $(Bi_xSb_{1-x})_2Te_3$ are studied, for which a topological transition to a 2D topological QSH insulator phase has been proposed. Indeed, an edge state in the LDOS is observed within the band gap. Yet, in nanoscale transport experiments with a four-tip STM, two-quintuple-layer films do not exhibit a ballistic conductance in the edge channels and thus no QSH edge states. This demonstrates that the detection of edge states in spectroscopy can be misleading with regard to the identification of a QSH phase. In contrast, nanoscale multi-tip transport experiments are a robust method for effectively pinpointing ballistic edge channels, as opposed to trivial edge states, in quantum materials.

1. Introduction

A quantum spin Hall (QSH) phase is characterized by a band gap in its 2D interior and by 1D, counter-propagating, and

spin-polarized helical edge states.[1,2] Inducing superconductivity in QSH edge states provides routes to engineering topological superconductivity, with potential applications in topological quantum computing.[3,4] So far, the QSH phase has been realized, for example, in semiconductor quantum wells[5] and monolayer transition metal dichalcogenides.[6-8] The unequivocal identification of the QSH phase in a given material requires the confirmation of two experimental signatures: an electronic band gap in the bands of the 2D interior, and spin-polarized helical edge states with a ballistic conductance around the perimeter of the topological phase, that is, at the boundaries to topologically trivial matter or vacuum.

Although local probes, such as scanning tunneling spectroscopy (STS), are powerful tools to characterize the bulk band gap and the LDOS of possible edge states, [9] such measurements cannot provide sufficient evidence for a QSH phase. The LDOS of an edge state is at most a necessary, but certainly not a sufficient

condition for its existence. In contrast, a ballistic edge conductivity constitutes a much more robust signature of a QSH phase, if it can be measured reliably. The latter is indeed challenging,

A. Leis, V. Cherepanov, B. Voigtländer, F. Lüpke, F. S. Tautz Peter Grünberg Institut (PGI-3) Forschungszentrum Jülich 52425 Jülich, Germany E-mail: b.voigtlaender@fz-juelich.de

The ORCID identification number(s) for the author(s) of this article can be found under https://doi.org/10.1002/qute.202200043

© 2022 The Authors. Advanced Quantum Technologies published by Wiley-VCH GmbH. This is an open access article under the terms of the Creative Commons Attribution License, which permits use, distribution and reproduction in any medium, provided the original work is properly cited.

DOI: 10.1002/qute.202200043

A. Leis, M. Schleenvoigt, V. Cherepanov, P. Schüffelgen, G. Mussler, D. Grützmacher, B. Voigtländer, F. Lüpke, F. S. Tautz Jülich Aachen Research Alliance (JARA) Fundamentals of Future Information Technology 52425 Jülich, Germany
A. Leis, B. Voigtländer, F. S. Tautz Experimentalphysik IV A RWTH Aachen University
Otto-Blumenthal-Straße, 52074 Aachen, Germany

M. Schleenvoigt, K. Moors, P. Schüffelgen, G. Mussler, D. Grützmacher Peter Grünberg Institut (PGI-9) Forschungszentrum Jülich 52425 Jülich Germany

52425 Jülich, Germany H. Soltner

Zentralinstitut für Engineering Elektronik und Analytik (ZEA-1) Forschungszentrum Jülich 52425 Jülich, Germany

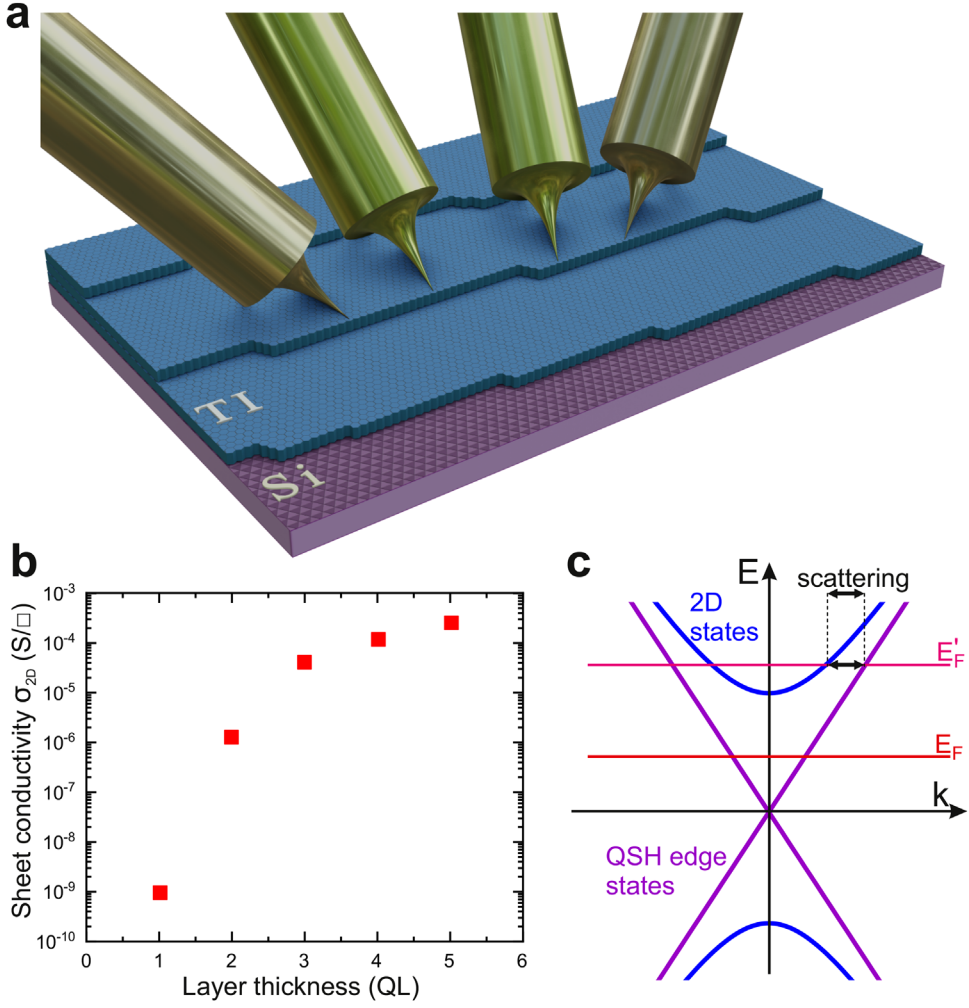


Figure 1. Schematic sketch of the sample layout and the principle of non-invasive nanoscale transport measurements with freely positionable contacts. a) Due to the shadow mask technique employed during the MBE growth of the sample, the boundary region of the TI film forms a wedge, consisting of terraces terminated by single-layer step edges. The positioning of the tips of the four-tip STM parallel or perpendicular to the step edges and their use as electrical probes allows transport measurements involving possible edge states. Since the 2D sheet conductivities σ_{2D} of each terrace are known, the contribution of the edge states to the overall charge transport can be identified. b) Terrace sheet conductivities σ_{2D} of (Bi_{0.16}Sb_{0.84})₂Te₃ thin films as a function of thickness, measured in quintuple layers (QL). Data are reproduced from reference.^[22] c) Schematic band structure of a 2D TI film. Due to the interaction between top and bottom TSS of the underlying 3D TI, a band gap forms in the two-dimensional interior of the film; corresponding states are shown in blue. At the edges of the 2D TI, topologically protected QSH edge states may form (purple). If the Fermi level is located in the gap (E_F), the transport in them is expected to be ballistic, while the film interior shows a comparatively low sheet conductivity σ_{2D} . If the Fermi level is located outside the gap (E_F), σ_{2D} is larger and inter-band scattering may destroy the ballistic conductivity in the QSH edge states.

because ultra-thin films are difficult to prepare with well-defined edges, and moreover they are sensitive to degradation in ambient conditions and lithographic processing. These adversities can distort or even mask the QSH effect, especially if the transport measurements provide no information on the spatial distribution of the electrical current—a common disadvantage of standard electrical transport measurements with lithographic contacts. A clearcut proof of a QSH phase in real systems is therefore facilitated considerably by a combination of nanoscale imaging, local spectroscopy, and local transport characterization, ideally under in situ conditions. This unique portfolio is only offered by multi-tip scanning tunneling microscopy (STM), in which each tip serves as a mobile electrical probe, [10] as shown in Figure 1a.

Whereas the QSH phase was first observed in HgTe quantum wells, $^{[5]}$ the weakly coupled nature of the layered van der Waals material ($\mathrm{Bi}_x\mathrm{Sb}_{1-x}$) $_2\mathrm{Te}_3$ (BST) allows direct access to the topological surface states for studying their detailed properties, and BST also allows a more flexible integration of the QSH phase into devices with other materials. Here, we use multi-tip STM to study edge state conductances in few-layer BST films. In the bulk limit, BST is a 3D topological insulator (TI) with 2D topological surface states (TSS) and a bulk band gap of about 300 meV. $^{[11-14]}$ However, when thinned down to a few quintuple layers (QL), the TSS at the top and bottom surfaces of the film begin to hybridize, resulting in a topological transition to either a QSH or a trivial insulator, depending on the material composition. $^{[15-19]}$

Both topological phase transitions are accompanied by the opening of a gap at the TSS Dirac points, but in contrast to the topologically trivial phase, the QSH phase guarantees the presence of topological edge states and corresponding ballistic conductance channels (Figure 1c).

The opening of a gap at the TSS Dirac point of BST in the few-QL limit was observed by both by photoemission spectroscopy and STS.[9,20,21] Moreover, four-point resistance measurements on individual terraces of a BST sample showed an approximately exponential drop of the sheet conductivity with decreasing film thickness,[22] as displayed in Figure 1b. But the observation of the hallmark of a QSH phase, that is, a ballistic conductance in a topological edge state, has not yet been confirmed in this material system. Due to the required lithographic patterning of electrical contacts, which results in the immediate degradation of the ultra-thin films,[23] such measurements are very challenging in the standard methodology of transport experiments. With our multi-tip STM approach, however, we circumvent this problem elegantly and are able to access the electrical properties of the pristine edge states in situ, without the need for lithographic processing.

We have chosen a Sb-rich ternary BST compound, (Bi_{0.16}Sb_{0.84})₂Te₃, for our search of highly conductive edge states, because for this stoichiometry, the Fermi level is located within the bulk band gap.[22] It is well-known that the potential occurrence of a QSH phase in ultra-thin films depends both on the composition and the thickness of the film. For binary BST compounds, theoretical calculations predicted that only the 2 QL Bi₂Te₃ film supports a QSH phase,^[19] while other calculations predicted 3 QL Sb₂Te₃ to form a QSH phase under specific conditions.[17] Also, some experimental indication of a QSH phase in 3 QL Sb₂Te₃ was found.^[21] In our experiments, we confirm that 2 QL and 3 QL films with the composition (Bi_{0.16}Sb_{0.84})₂Te₃ do not exhibit highly conductive edge states. For 2 QL, we conclude that the film does not support a QSH phase. Notably, the absence of conducting edge states in our transport measurements occurs in spite of the spectroscopic identification of edge states, which therefore must be assigned to trivial ones, not exhibiting ballistic transport. This illustrates the value of our generic approach to the unambiguous pinpointing of topological edge states in quantum materials, although for the specific sample under study no such states could be identified.

2. Experiments

 $(Bi_{0.16}Sb_{0.84})_2Te_3$ thin films were grown on silicon-on-insulator (SOI) substrates by molecular beam epitaxy (MBE), using the same process as reported earlier. The use of SOI substrates with a thin top layer of intrinsic Si reduces the substrate sheet conductivity to about $2~nS\Box^{-1}$. To achieve a TI film with boundaries on the SOI substrate without the need of ex situ processing, growth was conducted through a removable shadow mask. In the boundary region of the latter, the TI film formed a wedge in which the thickness decreases in single-QL steps from the maximum of 12 QL (1 QL \approx 1 nm) down to the bare Si(111) template layer, as indicated in Figure 1a. Regarding the stoichiometry at boundary region of the film, the rotation of the sample plus the mask during growth and the mobility of the deposited materials maintains

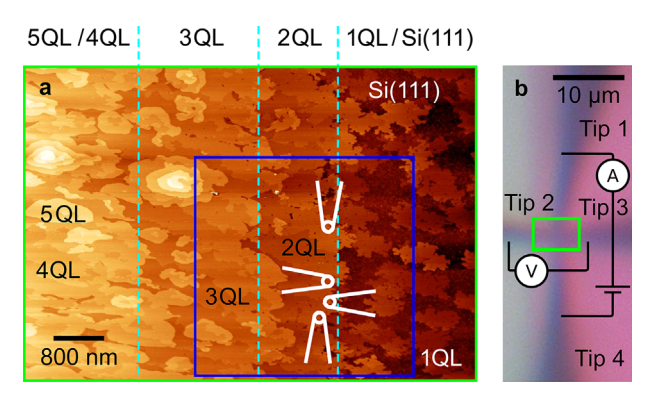


Figure 2. Topography of the $(Bi_{0.16}Sb_{0.84})_2Te_3$ film and exemplary measurement configuration. a) A large overview STM scan is performed with one of the tips to map the topography of the TI film close to its boundary. The image shows single-QL steps (cyan dashed lines), thus revealing the wedge-shaped structure of the film down to the Si(111) substrate. Film thicknesses are labeled above the map. The overview scan serves as a reference map to place all four tips (white symbols) in the vicinity of a selected step edge (here: 1 QL / 2 QL). The blue square indicates the image frame of Figure 4a. b) Optical microscope image of the final tip configuration. The area of the overview STM scan is indicated by the green rectangle.

a constant stoichiometry. For instance, the sample rotation removes penumbra effects which could otherwise arise from different evaporators or due to the finite height of the mask. After the growth, vacuum transfer with $p \le 1 \times 10^{-9}$ mbar was carried out to load the sample into the room temperature four-tip STM ($p \le 4 \times 10^{-10}$ mbar). The vacuum transfer, as well as the fact that electrical transport measurements using a four-tip STM do not require any additional sample processing beyond the growth, both preserve the pristine TI film, thus avoiding any influence of passivation or lithography steps on the charge transport properties. [23] After the electrical measurements, ex situ Rutherford backscattering measurements were performed to determine the precise atomic composition of the ternary compound.

All STM, STS and nanoscale four-point transport measurements reported here were performed in the Jülich room-temperature multi-tip STM. [24] Topographic STM images and dI/dV-images were recorded in constant-current mode with the bias voltage $V_{\rm b}$ applied to the sample. The spectroscopic dI/dV signal was acquired using standard lock-in techniques with a modulation frequency f=320 Hz and amplitude $V_{\rm mod}=30$ mV. To first order, dI/dV(E) is proportional to the LDOS at the local probe position and at energy $E=eV_{\rm b}$ with respect to the Fermi level of the sample. [25] Electrochemically etched tungsten wires were used as STM tips.

To perform electrical four-point measurements with the multitip STM, the four tips were brought to the desired positions on the sample surface by scanning the region of interest in tunneling contact. They were then lowered from the tunneling regime into contact with the sample surface, thereby establishing electrical point contacts to the TI film.^[26] After the electrical measurements, the tips were lifted from the sample surface and subsequent topography scans showed that the contact points of the tips are discernible only as small spots which do not influence the measured four-point resistance significantly (see Supporting Information).

www.advquantumtech.com

In the present experiments, placing the tips close to the step edges of the MBE-grown wedge-like film is a particular challenge. To meet the required level of precision in placing the tips at a selected step edge, we employed a positioning technique relying on successive STM scans performed with all tips, [26] which is discussed in exhaustive detail in ref. [27]. In a first step, we used the optical microscope to position the tips roughly above the boundary region (Figure 2b). Then, we approached the tips into the tunneling regime and measured overview scans of the topography of the TI film. Figure 2a shows such a large overview scan performed with one of the tips in the boundary region of the film, indicating the approximate extent of the terraces by the dashed blue lines. After all tips had been moved into the mapped boundary region (green rectangle in Figure 2b), using optical microscope imaging, small-scale STM scans were recorded with each tip to find topographic features that were also seen in the large overview scan. Once a topographic feature had been recognized, the position of the corresponding scanning tip was known. Further adjustments of each tip position were then achieved by fine lateral movement using piezoelectric control in tunneling contact.^[27] In this manner, all tips were placed in a desired position, as shown exemplary by the white symbols in Figure 2a. More details on the accuracy of the determination of the tip distances can be found in Supporting Information.

In the ensuing transport experiment, the outer two STM tips injected a charge current, while the inner tips probed the resulting electrochemical potential. The four-point resistance for a given tip arrangement was measured by recording the four-probe I-V characteristics, with currents of up to 10 μ A. In all measurements, only the position of one of the voltage-probing tips was varied, while the other tips were kept in fixed locations.

3. Results and Discussion

3.1. Spectroscopic Evidence for Edge States

Edge states typically show an increased LDOS which can be detected in STM and STS. For the example of topologically protected edge states, this was demonstrated, for example, in refs. [28–32]. **Figure 3**a shows an STM topography image of a region close to a step edge between a 3 QL and a 4 QL film, and in Figure 3b–i, corresponding constant-energy dI/dV maps are displayed. At energies larger than 220 meV, the maps convey a uniform density of states. Specifically, they exhibit no edge features. Yet, for energies below 220 meV, a distinct LDOS signal along the step edges is observed. Since it occurs at the same magnitude regardless of whether the scanning tip ascends to the 4 QL terrace or descends to the 3 QL terrace (both types of tip trajectories are present in Figure 3), we can rule out the possibility that the dI/dV signal at the step edge is due to a feedback artifact.

From angle-resolved photoemission spectroscopy (ARPES), it is known that the Fermi level at the top surface of thicker (Bi $_{0.16}$ Sb $_{0.84}$) $_2$ Te $_3$ films is located 50 meV above the TSS Dirac point and about 200 meV below the bulk conduction band, as estimated by interpolation of ARPES data in ref. [22] and refs. [21] and [24] therein. Therefore, the spectroscopic energy range of $0 \lesssim eV_b \lesssim$ 200 meV should correspond to states in the bulk band gap. Thus, we can conclude that the increased LDOS at the step edges in Figure 3f–i must belong to states in the bulk

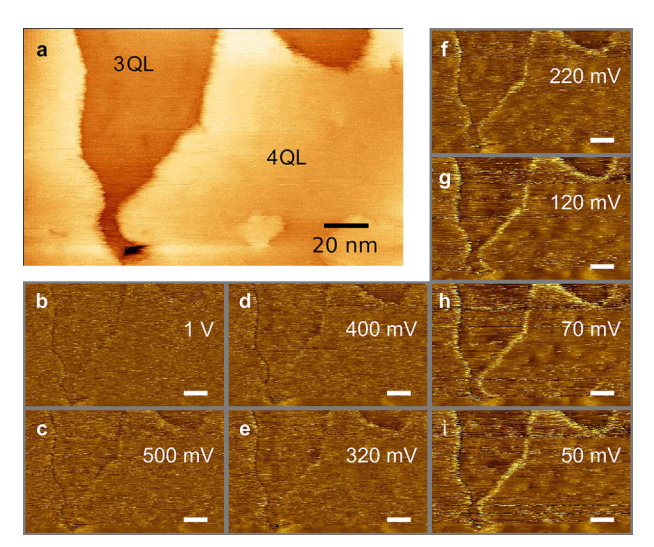


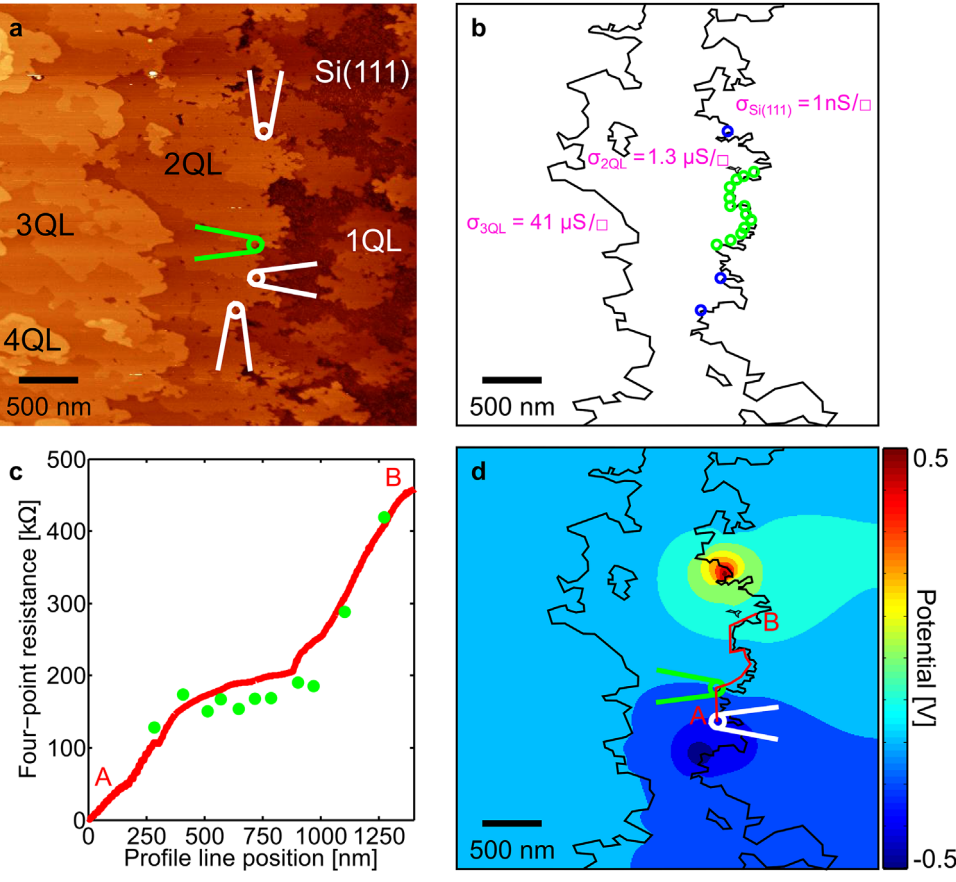
Figure 3. Differential conductance maps close to a step edge of the $(Bi_{0.16}Sb_{0.84})_2Te_3$ film. a) STM topography scan of the investigated area, including a step edge between a 3 QL terrace and a 4 QL terrace. b—i) Corresponding spectroscopic dI/dV maps, recorded in constant current mode at different sample bias voltages between 1 V and 50 mV. A pronounced feature in the dI/dV signal along the step edge at voltages below 220 mV indicates an increased LDOS at the step edge, thus an edge state.

band gap. The fact that these features disappear at a somewhat higher energy (about 220 meV) than expected may be explained by a thickness-dependent bulk band gap^[9] which might easily increase by about 20 meV for thin films of 3–4 QL.

Characteristic LDOS signals at step edges as observed here are also found in other systems and have been interpreted as nontrivial QSH edge states. [28-32] Following this argumentation, we might conclude from Figure 3 that the 3 QL (Bi_{0.16}Sb_{0.84})₂Te₃ film constitutes a QSH phase, while the 4 QL film is topologically trivial (or vice versa), leading to a 1D topological edge state at the boundary between the two. It must be noted, however, that from spectroscopic data alone it is not clear whether observed edge states are in fact topologically nontrivial. Therefore, it is necessary to explicitly prove the topological nature of spectroscopically observed edge states. One way to achieve this is the measurement of the electrical conductance in these edge states. If an edge state is topological, then electrons injected into it should be protected from scattering and therefore travel ballistically along the edge, even if it is rugged. [33] This will lead to conductances that are substantially larger than the reference conductance in the 2D interior (i.e., on the terraces) of the film.

In the remainder of the paper, we will follow this approach, using a four-tip STM with which ballistic transport signatures in edge channels can in principle be detected by spatially resolved resistance measurements. [34–37] As mentioned above, in the present case the challenge is to precisely position our STM tips as close as possible to the rugged step edges of the MBE-grown wedge-like $(\mathrm{Bi}_{0.16}\mathrm{Sb}_{0.84})_2\mathrm{Te}_3$ film. With the methodology described in the section Experiments, we have been able to overcome this difficulty and have performed distance-dependent four-point resistance measurements in close vicinity to the step edges.





corresponds to the blue square in Figure 2a. White symbols indicate the positions of the current-injecting tips (top and bottom) and the fixed voltageprobing tip. The green symbol indicates the mobile voltage-probing tip. All tips are contacting the step edge between the 2 QL terrace and the Si(111) substrate. b) Outline of the step edges with terrace sheet conductivities indicated. [22] Fixed and mobile tip positions are indicated by blue and green open circles, respectively. c) Measured four-point resistance R_{2D}^{4P} (green circles) versus position along the step edge between points A and B, exhibiting an approximately linear distance dependence (\geq 100 k Ω µm⁻¹), in comparison with the result of a finite-element simulation without a highly conductive edge channel (red curve). d) Color plot of the electric potential $\phi(x, y)$ from the finite-element simulation. The step edges are highlighted as black lines. The white tip symbol indicates the fixed voltage-probing tip at A, the red symbol the mobile voltage-probing tip at the first of the green data points in (c). The trajectory of the mobile voltage-probing tip is indicated by the red line.

We add one last note regarding the connection between transport measurements and the spectroscopic measurements. Since a QSH edge state, if it exists, will occur throughout the whole TSS band gap (cf., Figure 1c), it will also be detectable in spectroscopic measurements away from the Fermi level, for example at 50 meV above $E_{\rm F}$, although the transport measurement is always carried out at $E_{\rm F}$.

3.2. Step-Edge Conductance by Four-Point Resistance Measurements along a Step Edge

Principally, there are several four-point measurement geometries in which ballistic edge channels can be identified. In this section, we use a geometry in which all four tips are lined up along a step edge to search for a possible ballistic conductance channel at the boundary of a 2 QL $(Bi_{0.16}Sb_{0.84})_2Te_3$ film to the bare Si(111) substrate. We note that the step edge does not need to be straight, as edge states of a QSH insulator are expected to retract from disordered edges into the 2D interior with a larger degree of straightness.[33] The STM image in Figure 4a shows the corresponding step edge and a representative measurement configuration of the four tips (white and green symbols). The precise sequence of measurement positions of the mobile voltage-probing tip is shown Figure 4b (green open circles). In Figure 4c, the measured four-point resistances are plotted versus the position of the mobile voltage-probing tip along the curved profile line (green dots). We observe a kink at the profile line position about 1 μm, with different linear slopes to left and right of the kink.

Already a straightforward qualitative analysis reveals that the data in Figure 4c are not consistent with the existence of a ballistic edge channel along the step edge. Since there can be no potential drop in a ballistic channel, [38] its four-point resistance should be independent of the distance between the voltage probes. This clearly is in contradiction with the measured data. Moreover, also the magnitude of the observed four-point resistance is at odds with what would be anticipated for a ballistic conductance channel. For a single, that is, not spin-degenerate,



ballistic channel, one expects four-point resistances between $R_b^{4P}=0$ and $R_b^{4P}=h/e^2=25.8~k\Omega$ for the limiting cases of noninvasive and invasive voltage probes, respectively.^[34,36] The significantly higher four-point resistances that we measure in our experiment ($\geq 100~k\Omega~\mu m^{-1}$) strongly suggest that there is no ballistic conductance channel at the step edge in Figure 4a.

It should be noted, however, that a QSH phase could in principle also exhibit a behavior that is devoid of ballistic transport signatures. This would be the case if the Fermi level were not in the TSS band gap or if inelastic scattering were present. In the first case, interband scattering could occur between the 1D edge channel and the states in the 2D interior, as shown in Figure 1c. As a result, the conductance in the edge channel would be reduced. Because the Fermi level position in the bands of the 2D film interior would at the same time increase the 2D sheet conductivity, an existing ballistic conductance channel at the edge could in fact be masked in our transport experiments, and with it a QSH phase in the film. However, because of the large TSS band gap $\Delta_{2.01} \approx 250 \text{ meV}$, [9,19] which opens approximately symmetric with respect to the TSS Dirac point, and the Fermi level position $E_{\rm F} \approx 50$ meV above the TSS Dirac point^[22] (with a spread of about 25 meV at room temperature), the Fermi level will be located within the TSS band gap and thus inter-band scattering seems very unlikely here. Regarding the second case, it should be noted that inelastic scattering, for example, by electron-phonon interaction, is possible in principle, even if elastic backscattering of the spin-polarized QSH edge states is excluded by timereversal symmetry. Obviously, inelastic scattering could increase the resistance of the edge channel beyond what is expected for the ballistic case. The strength of this effect depends on the particular system, but has not yet been quantified at conditions close to room temperature. Usually, the opposite behavior is observed, namely that the resistance decreases as a function of temperature due to thermal activation of transport in 2D bulk states. [8,39] However, in our experiment, bulk transport is strongly suppressed at room temperature (in particular for the 2 QL terrace), which imposes stringent conditions on the inelastic scattering rate that would be required to obtain a QSH edge state with a resistivity of up to $\geq 100\, k\Omega~\mu m^{-1}.$ Therefore, the absence of a QSH edge state remains the most convincing explanation for the experimental data.

Having all but ruled out the presence of ballistic conductance channels at the edge of the 2 QL film, we still need to explain the distinctive behavior of the four-point resistance in Figure 4c. To this end, we performed a finite-element simulation of a classical boundary value problem, taking into account the precise shape of the terraces from Figure 4a, the exact positions of the current injection points (at which the potential in the calculation was set to +0.5 and -0.5 V), and the known sheet conductivities^[22] of both the 2 QL $(\mathrm{Bi}_{0.16}\mathrm{Sb}_{0.84})_2\mathrm{Te}_3$ film and the Si(111) substrate, $\sigma_{2\,\mathrm{QL}}=1.3~\mu\mathrm{S}\Box^{-1}$ and $\sigma_{\mathrm{Si}(111)}=1~\mathrm{nS}\Box^{-1}$. The resultant distribution of the electric potential ϕ in the film surface is displayed in Figure 4d. From this calculated potential, we extracted the fourpoint resistance $R_{\rm 2D}^{\rm 4P} = \delta \phi/I$ measured between the fixed and the mobile voltage-probing tips at different positions along the step edge (red line in Figure 4d and red curve in Figure 4c), where $\delta \phi$ is the calculated potential difference between points at which voltage-probing tips are placed and I is the current. We note the excellent agreement of the experimental and simulated fourpoint resistances (without any scaling factor). Even the kink in the four-point resistance around 1 μ m along the step edge is faithfully reproduced in the simulation. This implies that this feature originates from the specific shape of the step edge, and does not require any change in local conductivities within the film for its explanation, as would be instigated, for example, by a ballistic conductance channel at the edge of a QSH phase. All the evidence put together, we thus unequivocally conclude that the present 2 QL film of $(Bi_{0.16}Sb_{0.84})_2Te_3$ does not exhibit ballistic edge channels and, since the neighboring Si substrate is definitely topologically trivial, also does not represent a QSH phase either.

An analysis of the band structures of both Bi₂Te₃ and Sb₂Te₃ in the thin-film limit with many-body perturbation theory in the socalled GW approximation has revealed that 2 QL films of Bi₂Te₃ are expected to be a QSH insulator, with a TSS band gap of 0.15 eV.[19] With a gap of this size, the edge channels should be observable in experiment, if indeed the Fermi level is in the TSS band gap. The fact that we do not observe this QSH phase in our transport experiment does not necessarily contradict this result, because in the same calculation 2 QL films of Sb₂Te₃ are found to be topologically trivial, [19] and it is not a priori clear how the mixed compound $(Bi_{0.16}Sb_{0.84})_2Te_3$ would behave, although one might expect it to resemble Sb₂Te₃ more closely than Bi₂Te₃. Therefore, we have also carried out nanoscale four-point transport experiments on 2 QL films of Bi₂Te₃ in order to search for a ballistic conductance channel along the edges. Because of the intrinsic *n* doping of this material, however, this requires to shift the Fermi level from the 2D conduction band into the TSS band gap. Since our samples are MBE-grown on silicon-on-insulator substrates, this can principally be achieved by gating.^[22] Unfortunately, however, no change of the sheet conductivity upon gating up to 200 V was observed in initial experiments, showing that our gating capability is not sufficient to move the Fermi level into the TSS band gap of Bi₂Te₃. As a result, the terrace conductivity of this sample was significantly higher ($\approx 200 \, \mu \text{S} \square^{-1}$) than that of $(Bi_{0.16}Sb_{0.84})_2Te_3$, $(1.3 \mu S\Box^{-1})$, such that we were unable to distinguish any edge conduction. However, this does not mean that the Bi₂Te₃ films are topologically trivial. It just illustrates our inability to suppress their 2D sheet conductivities sufficiently.

3.3. Step-Edge Conductance by Four-Point Resistance Measurements across a Step Edge

Although the results of the analysis in the previous section are unambiguous, one may ask how critical it is to bring the tips as close as possible to the step edge (and thus also to the edge state) in order not to miss the ballistic edge channel whose width is difficult to gauge. In this section, we therefore explore whether a tip configuration with less stringent requirements can be used to identify the presence or absence of a ballistic edge channel as well. Specifically, we position three tips moderately close and roughly parallel to a step edge, while the fourth, that is, one of the voltage-probing tips, is moved through a sequence of measurement positions along a line that runs approximately perpendicular to the step edge. We apply this measurement geometry to the same sample as before, but we focus on the step edge between the 2 QL and 3 QL films. Since we have already established

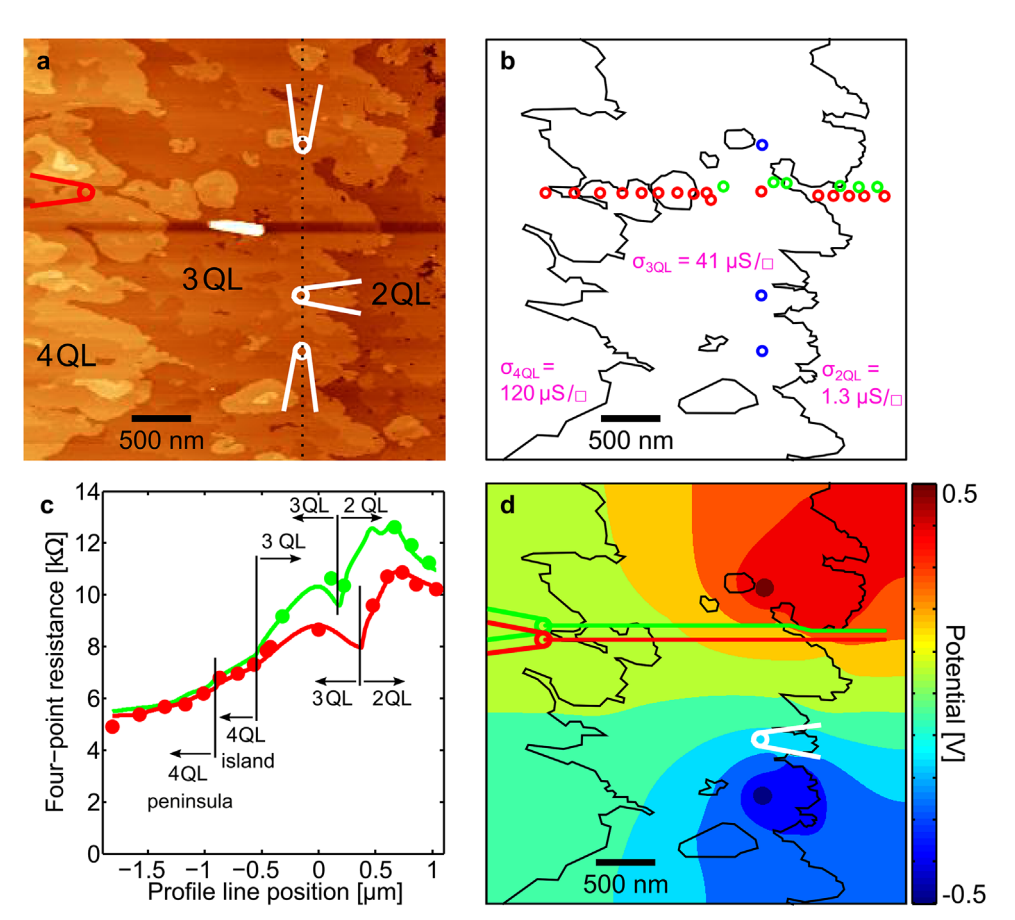


Figure 5. Four-point resistance measurements perpendicular to a step edge. a) STM topography image of the investigated ($Bi_{0.16}Sb_{0.84}$)₂Te₃ film. White symbols indicate the positions of the current-injecting tips (top and bottom) and the fixed voltage-probing tip. The red tip symbol indicates the mobile voltage-probing tip. While the static STM tips are placed along the step edge between the 3 QL and 2 QL terraces, the mobile voltage-probing tip is moved perpendicularly to the step edge. b) Outline of the step edges with terrace sheet conductivities indicated.^[22] Fixed tip positions are indicated by blue, mobile tip positions by red and green open circles. c) Measured four-point resistance R_{2D}^{4P} (red and green circles) versus position, in comparison with the result of a finite-element simulation without a highly conductive edge channel (red and green curves). Characteristic positions along the profile line are marked. d) Color plot of the electric potential $\phi(x, y)$ from the finite-element simulation without highly conductive channel. The step edges are highlighted as black lines. The white symbol indicates the fixed voltage-probing tip, the green/red symbol the mobile voltage-probing tip at the first of the red data points in (c). The trajectories of the mobile voltage-probing tips are indicated by the green/red lines.

that the 2 QL ($\mathrm{Bi}_{0.16}\mathrm{Sb}_{0.84}$)₂Te₃ film is trivial, we can thus analyze the topological properties of the 3 QL film.

Figure 5a shows an STM image of the boundary region between 2 QL and 3 QL terraces of the sample. The two currentinjecting tips and the immobile voltage-probing tip are placed on the 3 QL terrace along the vertical dotted line, at a distance of ≈ 200 nm from the step edge to the 2 QL terrace. The measurement positions of the mobile tip are indicated by red and green symbols in Figure 5b for two measurement series, which are slightly offset against each other. As before, we simulate the transport experiment by solving the corresponding boundary value problem with the known sheet conductivities.

The red and green curves in Figure 5c show the calculated four-point resistances along the two horizontal lines in Figure 5d. The agreement between the measured four-point resistances and the finite-element simulation is again exceptionally good, including details such as the maxima at $\approx 0.5~\mu m$, the dip in the green data set at $\approx 0.15~\mu m$, and the vertical offset between red and green data sets.

Whether the presence of a ballistic edge channel will modify the measured four-point resistances depends on the ratio of the terrace sheet conductivity $\sigma_{\rm 2D}$ to the total contact resistance $R_{\rm b}=h/e^2=25.8~{\rm k}\Omega$ involved in entering and leaving the ballistic conductance channel. If $1/\sigma_{\rm 2D}\gg R_{\rm b}$, the ballistic channel acts as a perfect conductor. Whenever this strong condition applies, the current path through the ballistic channel is strongly preferred over the current path through the plane, resulting in a significantly modified four-point resistance. In the opposite case, the contact resistance $R_{\rm b}$ will impede the current from entering the ballistic channel.

In the present case, the above-mentioned strong condition is not fulfilled, since $1/\sigma_{3\,\mathrm{QL}}\approx24\,\mathrm{k}\Omega\Box^{-1}$ is of the same order as R_b . However, there is a weaker condition which indicates that a significant part of the current flows through the ballistic channel. To illustrate this, consider a current injection into the plane at positions close to the potential ballistic edge channel (as in Figure 5a). In this case, the currents through the ballistic channel and the plane can be approximated by a parallel resistor model

www.advquantumtech.com

in which the resistance through the plane is given by its two-point resistance $R_{\rm 2D}^{\rm 2P}$. If the weaker condition $R_{\rm 2D}^{\rm 2P} > R_{\rm b}$ is fulfilled, the parallel resistor model tells us that a large part of the current flows through the ballistic channel, which influences in turn the measured four-point resistances.

The two-point resistance in a plane is given by^[10]

$$R_{\rm 2D}^{\rm 2P} = \frac{1}{\pi \sigma_{\rm 2D}} \ln \left(\frac{\Delta x - R}{R} \right) \tag{1}$$

where Δx is the distance between the current-injecting tips and R their contact radius. Considering the case in Figure 5a with $\Delta x \approx 1.7 \,\mu\text{m}$ and $R \approx 10 \,\text{nm}$, the two-point resistance on the 3 QL terrace results as $R_{2D}^{\rm 2P} \approx 40 \,\mathrm{k}\Omega$. The actual two-point resistance is expected to be nearly twice this value, if—as in the present case the tips are close to a terrace of low conductivity and thus only one half-plane contributes to the two-point sheet conductance. Thus, in our case the condition $R_{\rm 2D}^{\rm 2P} \approx 80\,{\rm k}\Omega > R_{\rm b} = 25.8\,{\rm k}\Omega$ is fulfilled and a significant modification of the measured four-point resistance is expected if a ballistic channel were present. The experimental data are therefore not consistent with the presence of a highly conductive edge channel at the step edge between the 2 QL and the 3 QL films. We note that according to the above argument, the identification of 1D ballistic conductance channels is easier if σ_{2D} is small—for this reason we have deliberately chosen a (Bi, Sb_{1-x})₂Te₃ compound that has its Fermi level in the TSS band gap, such that the charge carrier density and hence the background conductivity on the terraces is as low as possible.

However, a note of caution is in order: the TSS band gap of the 3 QL film ($\Delta_{3\,\mathrm{QL}} \approx 60$ meV) is much smaller than that of the 2 QL film. [9,19] Because the estimated Fermi level position of $E_{\rm F} \approx \pm 50$ meV with respect to the TSS Dirac point^[22] is in the same range as this band gap, inter-band scattering between the ballistic edge channel and the 2D interior of the film cannot be excluded with certainty. If the Fermi level were indeed located in the 2D conduction band, the inter-band scattering would reduce the edge state conductance; at the same time, the sheet conductivity of the 2D interior of the film would increase, making it difficult to identify signatures of the ballistic transport in our transport data. For the 3 QL $(Bi_{0.16}Sb_{0.84})_2Te_3$ film we can therefore conclude that, if the Fermi level is in gap, the film must be topologically trivial. If, however, the Fermi level is located in the 2D conduction band, no definite conclusion regarding the existence of a QSH phase can be reached.

3.4. Analytical Model of the Four-Point Resistance along an Edge between Half-Planes with Distinct Sheet Conductivities

The excellent agreement between the experimental data and the simulation in Figures 4c and 5c encourages a further analysis of specific features in the four-point resistance profiles. To this end, we calculated such profiles analytically for two generic situations, with and without the presence of a highly conductive edge channel. As we will see in this section, the four-point resistances in the two limiting situations differ strongly. In many cases, these qualitative differences will allow the classification of films as topologically non-trivial by a straightforward visual inspection of the measured distance-dependent four-point resistance profiles. We

note that the calculations in this section assume the validity of the condition $1/\sigma_{2D} \gg R_b$.

To calculate the four point resistance $R_{2D}^{4P} = \delta \phi / I$, we analytically determined the potential distribution $\phi(x, y)$ due to the stationary current distribution, from which the potential difference $\delta\phi$ between arbitrary positions of the two voltage-probing tips was obtained. We considered the following geometry (Figure 6a): The two current-injecting tips were placed at $(-x_0, y_0)$ and (x_0, y_0) . We assumed constant sheet conductivities σ_1 for $\gamma > 0$ and σ_2 for y < 0 (for simplicity, we omit the subscript "2D" from now on). Applied to the present problem, this corresponds to a step between two terraces of different heights at y = 0. Within this model, we considered two cases: If the step at y = 0 is topologically trivial, then the system is fully described by the two finite sheet conductivities, for which we assumed that $\sigma_1 > \sigma_2$ (for a stepped TI film this would mean that the film thickness for y > 0is higher). If on the other hand one of the films is in a QSH state, a ballistic conductance channel will run along the edge at y = 0; we accommodated this case into our model by letting $\sigma_2 \to \infty$ and restricting our solution to the half-plane y > 0.

The calculated potentials (see Methods Section for the derivation of the corresponding equations) are plotted in Figure 6b,c for two cases, one of them modeling the presence of a ballistic edge channel (Figure 6b), the other its absence (Figure 6c). Turning to Figure 6b first, we observe that the potential is distorted from the simple dipolar distribution that would be observed if the current were injected into an infinite 2D plane. The profiles perpendicular to the edge which are displayed in the bottom part of Figure 6b reveal a strong drop of the potential toward the edge and in particular a near-constant potential $\phi_1(x,y)\approx 0$ along the edge for $y\to 0$, to achieve continuity with $\phi_2(x,y)=0$ for y<0. Since constant potential indicates low resistance and thus large current densities, Figure 6b reveals that the injected current preferably flows through the ballistic edge channel.

In contrast, the situation without the ballistic edge channel, but with a poorly conducting half-plane $\gamma < 0$, leads to a very different distribution of the potential, as shown in Figure 6c for the specific case $\sigma_2 = 0.01\sigma_1$. In Figure 6c, the strong variation with x of the potential $\phi_1(x,y)$ for $\gamma \to 0$ indicates a large resistance along the edge. As a consequence, the current is not only inhibited from entering the poorly conducting half-plane, but is suppressed already for $\gamma > 0$ while γ approaches zero from above. We note that ϕ_2 drops again for increasingly negative γ away from the edge. However, the "resistance barrier" on both sides of the edge means that the actual current density there will be very small. The potential $\phi_1(\gamma \to 0)$ does not vanish, as it was in the case for a perfectly conducting channel at $\gamma = 0$.

When we compare the two situations in Figure 6b,c, it becomes clear that all experimental data reported in this paper resemble the situation in Figure 6c. On the one hand, this confirms that no indications of a ballistic edge channel are present for $(Bi_{0.16}Sb_{0.84})_2Te_3$. On the other hand, this also shows that the behavior of the analytical solution of a straight step edge goes a long way to providing a qualitative guide to the existence or non-existence of a ballistic edge channel and therefore a QSH phase, even in cases when the actual step edge is far from straight. We note in this context that for strongly defective step edges, the edge states of a QSH insulator are expected to retract away from the



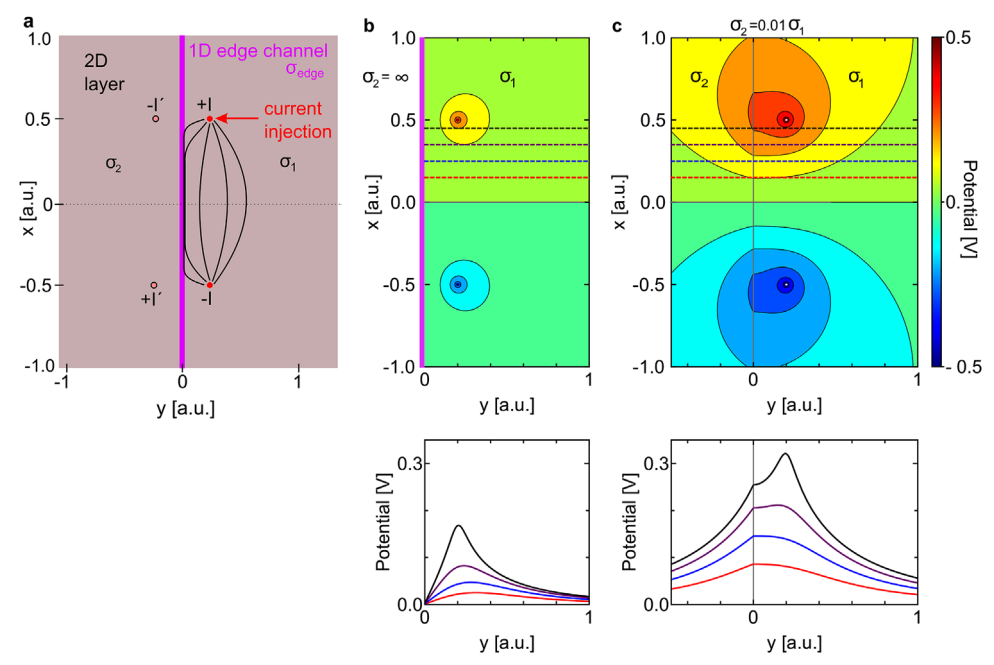


Figure 6. Analytical solution for the electric potential $\phi(x, y)$ close to the edge between two half-planes. a) Geometry of the boundary value problem. Two half-planes with sheet conductivites σ_1 (for $\gamma > 0$) and σ_2 (for $\gamma < 0$) meet at $\gamma = 0$. A current +1 is injected at (x_0, γ_0) and withdrawn (-I) at $(-x_0, \gamma_0)$. If $\sigma_2 \to \infty$, this geometry emulates the existence of a one-dimensional ballistic conductance channel at $\gamma = 0$ (magenta line). Positions of image current sources are indicated by I' (see Methods Section for more details). b) Color map of $\phi(x, \gamma)$ for $\sigma_2 \to \infty$. For $\gamma < 0$, the potential is zero. Profiles for $\gamma = 0$, the potential increases, reaches a maximum and falls to zero at the ballistic conductance channel. c) Color map and profiles of $\phi(x, \gamma)$ for $\sigma_2 = 0.01\sigma_1$, emulating the case of a step in the 2D sheet conductivity at $\gamma = 0$. The potential tends to increase toward this step, indicating the existence of a resistance barrier there.

step edge into the 2D interior, where the ballistic channel may preserve a larger degree of straightness.^[33]

There is, however, a further subtlety regarding modeling of QSH-derived ballistic edge channels by a terrace with infinite conductivity $(\sigma_2 \to \infty)$. In the QSH phase, the terrace and the edge state are decoupled, which means that current injection from the 2D terrace into the ballistic edge channel can only be realized through scattering processes. This gives rise to an effective contact resistance, which we, however, neglected in our analytical model on which the results of Figure 6b are based. But we expect that this effective contact resistance is small, for several reasons: First, the contact area is very large (it extends along the whole length of the terrace edge). Second, the interface between the 2D terrace and the edge state occurs within the same material and crystal structure, ruling out any interfacial barrier due to a material- or structure-based mismatch. And third, the substantial LDOS in the edge state, which is much larger than the LDOS in the terrace, enhances terrace-to-edge scattering over the terrace-to-terrace scattering. All of this will minimize the contact resistance between the 2D terrace and QSH edge channel. Moreover, due to the inevitable gap inversion between neighboring terraces that necessarily accompanies any QSH edge state, a considerable terrace-to-terrace contact resistance is expected. Thus, a high terrace-to-terrace contact resistance in connection with a small terrace-to-edge contact resistance allows the current to enter the ballistic edge channel effectively, permitting us to observe a possible QSH state as a highly conductive edge channel in our measurements. Note that this argument does not imply that the ballistic conductance in the edge channel is heavily modified

by terrace-to-edge coupling. From the perspective of the edge channel, the 2D states on both terraces only have a negligible LDOS near the edge. Hence, for a charge carrier in the QSH edge channel, the terrace-to-edge coupling is rather weak, and a significant effect on its ballistic conductance is not expected.

4. Conclusion

Employing the Jülich multi-tip STM, we performed nanoscale charge transport measurements in the vicinity of single quintuple-layer steps of TI films. Due to the precise positioning and navigation capabilities of our STM tips down to the nanoscale, we were able to spatially resolve four-point resistances at the surface of the TI film. Our local conductance data proved to be informative with respect to the presence or absence of ballistic edge channels that would indicate a QSH phase. In this sense, we achieved our goal to close the research gap between the spectroscopic characterization with scanning probe methods at the nanometer scale on the one hand, and conventional transport experiments at the micrometer scale on the other, even in the face of a nonideal nanoscale sample geometry (rugged edges).

From our experimental data, we could conclude that no ballistic edge channels were present in our sample for 2 QL films, despite a gap opening in the TSS of the underlying 3D TI, which manifested itself in an exponentially decreasing sheet conductivity for films with thicknesses below 5 QL and despite an edge state signature in the LDOS. Instead, we found that the measured four-point resistances agree quantitatively with results from finite-element simulations based on, first, the

actually observed intricate nanoscale sample geometry and, second, measured conductivities on the TI terraces. We also found qualitative agreement with an analytical solution of the Laplace equation in the idealized geometry of a straight edge at which no ballistic conductance channel is present.

The absence of ballistic edge channels implies a topologically trivial phase for a film thickness of 2 QL, for which $E_{\rm E}$ is clearly located in the TSS band gap. In contrast, for the film thickness of 3 QL, the absence of ballistic edge channels principally allows two interpretations: first, the absence of a QSH phase, or second, a QSH phase with topologically protected edge channels while $E_{\rm F}$ is located in the 2D conduction band. The latter situation would result in an enhanced terrace conductivity, while at the same time enabling scattering from the edge channel into bands of the 2D interior (see Figure 1c), thereby undermining the ballistic transport along the edges. We note, however, that a Fermi energy $E_{\rm F}$ in the 2D conduction band appears unlikely, because the terrace conductivity was found to be rather small for 3 QL films. Thus, we interpret the increased LDOS observed in dI/dVmaps at the step edges as originating from trivial edge states with a conductivity that is not higher than that of the surrounding terraces. In summary, we conclude that the investigated compound (Bi_{0.16}Sb_{0.84})₂Te₃ does not exhibit a QSH phase for 2 QL and probably also 3 QL films, because ballistic edge states, being the hallmark of a QSH phase, are not present. This is in agreement with theoretical predictions for the binary compound Sb₂Te₃ that is close to the stoichiometry of our present sample. [19]

On a more general note, we were able to demonstrate that STM-based multi-tip transport experiments are a powerful and generic method to search for ballistic edge channels. But we have also seen that firm conclusions could only be drawn with the provison that the Fermi level is located in the TSS band gap. This touches upon a problem of transport measurement in general, regardless of the methodology: if the bulk conductivity is too large, then it becomes difficult or impossible to distinguish the ballistic transport in the 1D edge channels from the transport in the 2D film interior. In this respect, the MBE-grown $(Bi_xSb_{1-x})_2Te_3$ films turned out to be problematic, because they require a certain stoichiometry to put the Fermi level into the bulk and TSS gap, but at the same time this stoichiometry influences the topological properties. In the near future, we therefore plan to apply the methodology of the present paper to exfoliated films, for which unintentional doping is expected to be less of a problem. Promising materials in this context are magnetic topological insulators, which exhibit a quantum anomalous Hall state, and van der Waals materials, such as the QSH insulator WTe₂, which allow an effective gate tuning. Moreover, low-temperature measurements could also reveal the impact of inelastic scattering on the transport properties of the edge channels. Finally we note that our technique is also compatible with the measurement of spin-polarized transport, if magnetic tips are used.^[26] This should finally bring us closer to the long-term goal of spin-polarized measurements of ballistic conductance channels with contacts that can be freely positioned on the nanoscale.

5. Methods Section

To interpret the experimental data, calculations of the electric potential distribution were performed for a given current injection geometry,

from which the four-point resistance between any two points in the sample plane can easily be determined. Two approaches were taken.

First, finite-element simulations were performed that took into account the measured terrace/step topography and the sheet conductivities on the respective terraces. [22] These simulations were carried out with the current flow module of the program OPERA 3D by Dassault Systèmes. [40] To build the simulation model, the precise step structure of the sample was first mapped into the simulation plane. Next, the simulation plane was extruded into the third dimension, using a uniform thickness of 25 nm of the simulation slab; in this process, the distinct heights of the terraces were not taken into account. Finally, each terrace was assigned a specific sheet conductivity. Since the simulation model is 3D, the sheet conductivity was distributed evenly across the thickness of the simulation slab. The maximum size of mesh elements in the simulation was set to 20 nm. The excellent agreement of the measured data with the simulation results justified this simplified approach.

Second, for the simple geometry of a conducting half-plane next to a straight edge channel with infinite conductivity, or next to a half-plane with negligible conductivity, the boundary value problem for a stationary current was solved analytically. [41] Following Ohm's law, the 3D current density j is given by $j=\hat{\sigma}E$, where E is the electric field and $\hat{\sigma}$ is the conductivity tensor, which was assumed to be diagonal and isotropic. With $E=-\nabla\phi$, one obtains

$$\Delta \phi = -\frac{\nabla \cdot \mathbf{j}}{\sigma} \tag{2}$$

This is a Poisson equation for the divergence $\nabla \cdot \mathbf{j}$ of the current density in full analogy to the common Poisson equation $\Delta \phi = -\rho/\epsilon_0$ for a charge density ρ .

In a first step, a point-like current injection at ${\bf r}_0\equiv 0$ into a plane is considered with constant σ everywhere. ${}^{[42]}$ Then, $\nabla\cdot {\bf j}({\bf r})=0$ for all ${\bf r}\neq 0$, and one has to solve the Laplace equation $\Delta\phi({\bf r})=0$ for ${\bf r}\neq 0$. Because of the symmetry of the problem, it is expedient to use cylindrical coordinates (ϱ,φ,z) in which the Laplace operator becomes $\Delta=\frac{1}{\varrho}\frac{\partial}{\partial\varrho}\varrho\,\frac{\partial}{\partial\varrho}+\frac{1}{\varrho^2}\frac{\partial^2}{\partial\varrho^2}+\frac{\partial^2}{\partial z^2}$. The second term vanishes for problems with cylindrical symmetry, while the third term can be neglected for 2D problems. Thus, for the present problem only the first term remains, and $\phi({\bf r})=\phi(\varrho)$ with $\varrho=|{\bf r}|=\sqrt{\chi^2+\gamma^2}$. One therefore

$$\frac{1}{\rho} \frac{\partial}{\partial \rho} \rho \frac{\partial}{\partial \rho} \phi(\rho) = 0 \tag{3}$$

with $\rho > 0$. Integrating twice, one obtains

$$\phi(\varrho) = c_1 \ln \varrho + c_2 \tag{4}$$

where c_1 and c_2 are integration constants. Since the potential is defined only up to an additive constant, one can set $c_2 = 0$. c_1 follows from the size of the injected current at $\rho = 0$. Placing a circle of radius R around the injection point (R can be taken as the contact radius of the tip) and integrating the now 2D current density f through this ring, one obtains

$$I = \oint_{L} (\mathbf{j} \cdot \mathbf{n}) d\mathbf{L} = \int_{0}^{2\pi} \mathbf{j}_{n}(\mathbf{R}) \mathbf{R} d\varphi = -2\pi\sigma \mathbf{c}_{1}$$
 (5)

where the circular symmetry and $j_n = -\sigma \frac{\partial \phi}{\partial \rho}(R) = \frac{c_1}{R}$ (Ohm's law and Equation (4)) has been used. Here, \mathbf{n} is the outer normal unit vector of the circle, and φ denotes the angle along its circumference L. Note that unlike in Equation (2), σ in Equation (5) is the 2D sheet conductivity, measured in S \Box^{-1} . One thus finally finds^[42]

$$\phi(\varrho) = -\frac{1}{2\pi\sigma} \ln \varrho = -\frac{1}{2\pi\sigma} \ln(\sqrt{x^2 + y^2}) = -\frac{1}{4\pi\sigma} \ln(x^2 + y^2)$$
 (6)

for the potential due to a single point-like current source +I at $\varrho=0$. In this case, the current -I is drained on a circular ring at $\varrho\to\infty$. In our experiment, however, the current drain -I occurs at the position of the second current-injecting tip. Hence, the radial current density distributions of both tips must be added to yield the total current density between the two tips. This corresponds to the summation of the potentials from these two tips to yield

$$\phi(x, y) = -\frac{1}{4\pi\sigma} \ln\left(\frac{(x - x_0)^2 + (y - y_0)^2}{(x + x_0)^2 + (y - y_0)^2}\right)$$
(7)

if +I is injected at (x_0, y_0) and -I is drained at $(-x_0, y_0)$ and the sheet conductivity σ is constant everywhere. Since the total current I is related to the applied voltage U by $I = U/R_{\rm 2D}^{\rm 2P}$, it follows that $\lambda \equiv I/\sigma = U(\rho_{\rm 2D}/R_{\rm 2D}^{\rm 2P})$, where $\rho_{\rm 2D} = \sigma^{-1}$ and the ratio in the brackets is given by Equation (1), yielding $\lambda = U\pi[\ln(\frac{\Delta x - R}{R})]^{-1}$.

The situation with a boundary at $\gamma=0$ at which σ changes, as shown in Figure 6a, was then considered. For $\gamma>0$, the potential ϕ_1 can be calculated by additionally injecting an image current +l' at $(-x_0, -\gamma_0)$ and withdrawing -l' at $(x_0, -\gamma_0).^{[41]}$ For $\gamma<0$, the potential ϕ_2 can be calculated without additional image currents, but with the original currents $\pm l$ at the injection points replaced by $\pm l''$, in order to account for the screening influence of the boundary at $\gamma=0.^{[41]}$ l' and l'' follow from the boundary conditions at the boundary $\gamma=0$ between to two half-planes. Specifically, because the current across the boundary must be continuous (no sources or drains in the boundary), one finds $\sigma_1 E_{\gamma,1} = \sigma_2 E_{\gamma,2}$ for the perpendicular electric field. Since the tangential electric field is continuous at any interface, $E_{\gamma,1} = E_{\gamma,2}$ holds. From these two conditions, one obtains $\lambda'=l'/\sigma_2=-\lambda(\sigma_1-\sigma_2)/(\sigma_1+\sigma_2)$ and $\lambda''=l''/\sigma_1=2\lambda\sigma_1/(\sigma_1+\sigma_2)$, where $\lambda=l'/\sigma_1$. The potential for $\gamma>0$ thus becomes

$$\phi_{1}(x, y) = -\frac{I}{4\pi\sigma_{1}} \left[\ln \left(\frac{(x - x_{0})^{2} + (y - y_{0})^{2}}{(x + x_{0})^{2} + (y - y_{0})^{2}} \right) + \frac{\sigma_{1} - \sigma_{2}}{\sigma_{1} + \sigma_{2}} \ln \left(\frac{(x - x_{0})^{2} + (y + y_{0})^{2}}{(x + x_{0})^{2} + (y + y_{0})^{2}} \right) \right]$$
(8)

while for y < 0

$$\phi_2(x,y) = -\frac{1}{2\pi(\sigma_1 + \sigma_2)} \ln\left(\frac{(x - x_0)^2 + (y - y_0)^2}{(x + x_0)^2 + (y - y_0)^2}\right)$$
(9)

holds. In the limit $\sigma_2 \to \infty$, one obtains

$$\phi_1(x,y) = -\frac{I}{4\pi\sigma_1} \ln \left(\frac{[(x-x_0)^2 + (y-y_0)^2][(x+x_0)^2 + (y+y_0)^2]}{[(x+x_0)^2 + (y-y_0)^2][(x-x_0)^2 + (y+y_0)^2]} \right)$$
(10)

and

$$\phi_2(x,y) = 0, \tag{11}$$

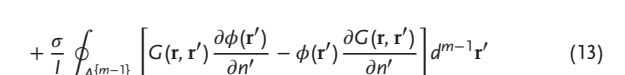
which corresponds to the case of a straight edge channel at y=0 with infinite conductivity.

Equation (7) can be written down immediately with the help of the Green's function $G(\mathbf{r}, \mathbf{r}')$ that fulfills the Poisson equation

$$\Delta G(\mathbf{r}, \mathbf{r}') = -\frac{1}{\sigma} \delta(\mathbf{r} - \mathbf{r}'). \tag{12}$$

In terms of the Green's function, the potential in an m-dimensional volume $V^{\{m\}}$ is given by $[^{43}]$

$$\phi(\mathbf{r}) = \int_{V^{\{m\}}} G(\mathbf{r}, \mathbf{r}') \frac{\nabla' \cdot \mathbf{j}(\mathbf{r}')}{l} d^m \mathbf{r}'$$



where the second integral extends over the surface $A^{\{m-1\}}$ surrounding the volume $V^{\{m\}}$. If this surface is located at infinity, then both $\phi(\mathbf{r}')$ and $\frac{\partial \phi(\mathbf{r}')}{\partial n'}$ vanish and with them the surface integral, the latter under the condition that $\phi(\mathbf{r}')$ and $\frac{\partial \phi(\mathbf{r}')}{\partial n'}$ vanish rapidly enough for $|\mathbf{r}'| \to \infty$; in the present context this means that the length increase of the integration contour must be compensated by a sufficient decrease of the integrand. In two dimensions, the Green's function of the Laplace operator in Equation (12) is given by [43]

$$G(\mathbf{r}, \mathbf{r}') = -\frac{1}{2\pi\sigma} \ln(|\mathbf{r} - \mathbf{r}'|) \tag{14}$$

The introduction of the point-like current sources at r_{\perp} and r_{\perp}

$$\nabla' \cdot \mathbf{j}(\mathbf{r}') = I\delta(\mathbf{r}' - \mathbf{r}_{+}) - I\delta(\mathbf{r}' - \mathbf{r}_{-})$$
(15)

into Equation (13) yields

$$\phi(\mathbf{r}) = -\frac{I}{2\pi\sigma} \ln\left(\frac{|\mathbf{r} - \mathbf{r}_+|}{|\mathbf{r} - \mathbf{r}_-|}\right) \tag{16}$$

which is identical with Equation (7), if $\mathbf{r}_+ = (x_0, y_0)$ and $\mathbf{r}_- = (-x_0, y_0)$.

Supporting Information

Supporting Information is available from the Wiley Online Library or from the author.

Acknowledgements

This work was supported by the German excellence cluster ML4Q (Matter and Light for Quantum Computing). Furthermore, the authors acknowledge the financial support by the Bavarian Ministry of Economic Affairs, Regional Development, and Energy within Bavaria's High-Tech Agenda Project "Bausteine für das Quantencomputing auf Basis topologischer Materialien mit experimentellen und theoretischen Ansätzen" (grant allocation no. 07 02/686 58/1/21 1/22 2/23). F.L. acknowledges funding by the Deutsche Forschungsgemeinschaft (DFG, German Research Foundation) within the Priority Programme SPP 2244 (project no. 443416235). F.S.T. acknowledges support of the Deutsche Forschungsgemeinschaft through the SFB 1083, project A12. The authors would like to thank R. Greven of ZEA-1 for the transfer of the STM data to the finite-element program

Open access funding enabled and organized by Projekt DEAL.

Conflict of Interest

The authors declare no conflict of interest.

Data Availability Statement

Data within the manuscript is available from the corresponding author upon reasonable request.

Keywords

ballistic conductivity, edge channel, multi-tip scanning tunneling microscopy, nanoscale charge transport, quantum spin Hall effect, topological insulator

[22] A. Leis, M. Schleenvoigt, V. Cherepanov, F. Lüpke, S. P., G. Mussler, D. Grützmacher, B. Voigtländer, F. S. Tautz, Adv. Quantum Technol.

2021. 4. 2100083.

- [23] P. Ngabonziza, R. Heimbuch, N. de Jong, R. A. Klaassen, M. P. Stehno, M. Snelder, A. Solmaz, S. V. Ramankutty, E. Frantzeskakis, E. van Heumen, G. Koster, M. S. Golden, H. J. W. Zandvliet, A. Brinkman, Phys. Rev. B 2015, 92, 035405.
- [24] V. Cherepanov, E. Zubkov, H. Junker, S. Korte, M. Blab, P. Coenen, B. Voigtländer, Rev. Sci. Instrum. 2012, 83, 033707.
- [25] B. Voigtländer, Scanning Probe Microscopy: Atomic Force Microscopy and Scanning Tunneling Microscopy, Springer, Berlin, Heidelberg 2015.
- [26] A. Leis, M. Schleenvoigt, A. Jalil, V. Cherepanov, G. Mussler, D. Grützmacher, F. S. Tautz, B. Voigtländer, Sci. Rep. 2020, 10, 2816.
- [27] A. Leis, V. Cherepanov, B. Voigtländer, F. S. Tautz, Rev. Sci. Instrum. 2022, 93, 013702.
- [28] C. Pauly, B. Rasche, K. Koepernik, M. Liebmann, M. Pratzer, M. Richter, J. Kellner, M. Eschbach, B. Kaufmann, L. Plucinski, C. M. Schneider, M. Ruck, J. van den Brink, M. Morgenstern, Nat. Phys. **2015**, 11, 338.
- [29] F. Reis, G. Li, L. Dudy, M. Bauernfeind, S. Glass, W. Hanke, R. Thomale, J. Schäfer, R. Claessen, Science 2017, 357, 287.
- [30] F. Lüpke, D. Waters, S. C. de la Barrera, M. Widom, D. G. Mandrus, J. Yan, R. M. Feenstra, B. M. Hunt, Nat. Phys. 2020, 16, 526.
- [31] S. Kim, K. Jin, J. Park, J. Kim, S. Jhi, H. Yeom, Sci. Rep. 2016, 6, 33193
- [32] Z. Alpichshev, J. G. Analytis, J.-H. Chu, I. R. Fisher, A. Kapitulnik, Phys. Rev. B 2011, 84, 041104.
- [33] S. Essert, K. Richter, 2D Mater. 2015, 2, 024005.
- [34] R. de Picciotto, H. Stormer, L. Pfeiffer, K. Baldwin, K. West, Nature 2001. 411. 51.
- [35] J. Baringhaus, M. Ruan, F. Edler, A. Tejeda, M. Sicot, A. Taleb-Ibrahimi, A.-P. Li, Z. Jiang, E. H. Conrad, C. Berger, C. Tegenkamp, W. A. de Heer, Nature 2014, 506, 349.
- [36] J. Aprojanz, I. Miccoli, J. Baringhaus, C. Tegenkamp, Appl. Phys. Lett. 2018, 113, 191602.
- [37] J. Aprojanz, S. R. Power, P. Bampoulis, S. Roche, A.-P. Jauho, H. J. W. Zandvliet, A. A. Zakharov, C. Tegenkamp, Nat. Commun. 2018, 9,
- [38] S. Datta, Electronic Transport in Mesoscopic Systems, Cambridge University Press, Cambridge 1995.
- [39] G. Dolcetto, M. Sassetti, T. L. Schmidt, La Rivista del Nuovo Cimento **2016**, 39, 113,
- [40] https://www.3ds.com/products-services/simulia/products/opera/ (accessed: July 2022).
- [41] J. D. Jackson, Classical Electrodynamics, 2nd Ed., Wiley, New York 1975.
- [42] S. Just, Dissertation, RWTH Aachen University, Forschungszentrum Jülich GmbH, Jülich, 2021.
- [43] G. Arfken, Mathematical Methods for Physicists, 3rd Ed., Academic Press, London 1985.

Received: April 28, 2022 Revised: June 27, 2022 Published online: August 2, 2022

- [1] B. A. Bernevig, S.-C. Zhang, Phys. Rev. Lett. 2006, 96, 106802.
- [2] M. S. Lodge, S. A. Yang, S. Mukherjee, B. Weber, Adv. Mater. 2021, 33, 2008029.
- [3] S. Das Sarma, M. Freedman, C. Nayak, npj Quantum Inf. 2015, 1, 15001
- [4] M. Sato, Y. Ando, Rep. Prog. Phys. 2017, 80, 076501.
- [5] M. König, S. Wiedmann, C. Brüne, A. Roth, H. Buhmann, L. W. Molenkamp, X.-L. Qi, S.-C. Zhang, Science 2007, 318, 766.
- [6] S. Tang, C. Zhang, D. Wong, Z. Pedramrazi, H.-Z. Tsai, C. Jia, B. Moritz, M. Claassen, H. Ryu, S. Kahn, J. Jiang, H. Yan, M. Hashimoto, D. Lu, R. G. Moore, C.-C. Hwang, C. Hwang, Z. Hussain, Y. Chen, M. M. Ugeda, Z. Liu, X. Xie, T. P. Devereaux, M. F. Crommie, S.-K. Mo, Z.-X. Shen, Nat. Phys. 2017, 13, 683.
- [7] Z. Fei, T. Palomaki, S. Wu, W. Zhao, X. Cai, B. Sun, P. Nguyen, J. Finney, X. Xu, D. H. Cobden, Nat. Phys. 2017, 13, 677.
- S. Wu, V. Fatemi, Q. D. Gibson, K. Watanabe, T. Taniguchi, R. J. Cava, P. Jarillo-Herrero, Science 2018, 359, 76.
- [9] Y. Jiang, Y. Wang, M. Chen, Z. Li, C. Song, K. He, L. Wang, X. Chen, X. Ma, Q.-K. Xue, Phys. Rev. Lett. 2012, 108, 016401.
- [10] B. Voigtländer, V. Cherepanov, S. Korte, A. Leis, D. Cuma, S. Just, F. Lüpke, Rev. Sci. Instrum. 2018, 89, 101101.
- [11] H. Zhang, C.-X. Liu, X.-L. Qi, X. Dai, Z. Fang, S.-C. Zhang, Nat. Phys. 2009, 5, 438.
- [12] Y. Xia, D. Qian, D. Hsieh, L. Wray, A. Pal, H.-H. Lin, A. Bansil, D. Grauer, Y. Hor, R. J. Cava, M. Z. Hasan, Nat. Phys. 2009, 5,
- [13] Y. L. Chen, J. G. Analytis, J.-H. Chu, Z. K. Liu, S.-K. Mo, X. L. Qi, H. J. Zhang, D. H. Lu, X. Dai, Z. Fang, S. C. Zhang, I. R. Fisher, Z. Hussain, Z.-X. Shen, Science 2009, 325, 178.
- [14] D. Hsieh, Y. Xia, D. Qian, L. Wray, H. Dil, F. Meier, J. Osterwalder, L. Patthey, J. G Checkelsky, N. P Ong, A. Fedorov, H.-H. Lin, A. Bansil, D. Grauer, Y. Hor, R. J Cava, M. Z. Hasan, Nature 2009, 460, 1101.
- [15] H.-Z. Lu, W.-Y. Shan, W. Yao, Q. Niu, S.-Q. Shen, Phys. Rev. B 2010, 81. 115407.
- [16] C.-X. Liu, H. Zhang, B. Yan, X.-L. Qi, T. Frauenheim, X. Dai, Z. Fang, S.-C. Zhang, Phys. Rev. B 2010, 81, 041307.
- [17] M. Kim, C. H. Kim, H.-S. Kim, J. Ihm, Proc. Natl. Acad. Sci. USA 2012, 109, 671.
- [18] T. Förster, P. Krüger, M. Rohlfing, Phys. Rev. B 2015, 92, 201404.
- [19] T. Förster, P. Krüger, M. Rohlfing, Phys. Rev. B 2016, 93, 205442.
- [20] Y. Zhang, K. He, C.-Z. Chang, C.-L. Song, L.-L. Wang, X. Chen, J.-F. Jia, Z. Fang, X. Dai, W.-Y. Shan, S.-Q. Shen, Q. Niu, X.-L. Qi, S.-C. Zhang, X.-C. Ma, Q.-K. Xue, Nat. Phys. 2010, 6, 584.
- [21] T. Zhang, J. Ha, N. Levy, Y. Kuk, J. Stroscio, Phys. Rev. Lett. 2013, 111, 056803.